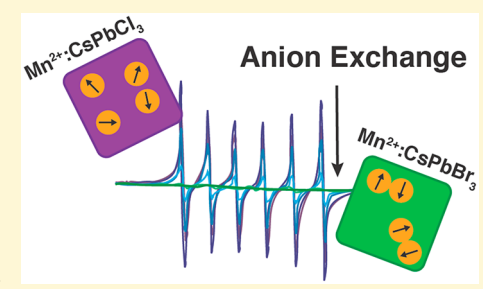


# Spinodal Decomposition During Anion Exchange in Colloidal Mn<sup>2+</sup>-Doped CsPb $X_3$ (X = Cl, Br) Perovskite Nanocrystals

Michael C. De Siena,<sup>†</sup> David E. Sommer,<sup>‡</sup> Sidney E. Creutz,<sup>†,⊥</sup> Scott T. Dunham,<sup>§</sup> and Daniel R. Gamelin\*,†

Supporting Information

ABSTRACT: Manganese(II)-doped cesium-lead-chloride (Mn<sup>2+</sup>:CsPbCl<sub>3</sub>) perovskite nanocrystals have recently been developed as promising luminescent materials and attractive candidates for white-light generation. One approach to tuning the luminescence of these materials has involved anion exchange to incorporate Br<sup>-</sup>, but the effects of anion exchange on Mn<sup>2+</sup> speciation in doped metal-halide perovskites is not well understood at a microscopic level. Here, we use a combination of X-band electron paramagnetic resonance (EPR) and photoluminescence spectroscopies to monitor the Mn<sup>2+</sup> dopants in Mn<sup>2+</sup>:CsPbCl<sub>3</sub> nanocrystals during Cl<sup>−</sup> → Br<sup>−</sup> anion exchange. Analytical measurements show that the nanocrystals retain their Mn<sup>2+</sup> over the course of



 $Cl^- \to Br^-$  anion exchange and they continue to show strong  $Mn^{2+}$  d-d luminescence but, surprisingly, the  $Mn^{2+}$  EPR intensities all but vanish. Further results suggest that Mn<sup>2+</sup> ions migrate during anion exchange to form clusters that are still luminescent but show no EPR signal due to antiferromagnetic superexchange coupling. Monte Carlo simulation and analysis of the  $Mn^{2+}$ :CsPb( $Cl_{1-x}Br_x$ )<sub>3</sub> lattice at various halide compositions (x) bolsters this interpretation by indicating a propensity for Mn<sup>2+</sup>-Cl<sup>-</sup> units to cluster as the Br<sup>-</sup> content increases, increasing the probability of the nearest-neighbor Mn<sup>2+</sup>-Mn<sup>2+</sup> interactions. The driving force for this clustering is retention of the stronger Mn-Cl bonds compared to Mn-Br bonds. In addition, modeling predicts spinodal decomposition to form  $Mn^{2+}$ -enriched domains even at the end point compositions of x =0 and 1, with Mn<sup>2+</sup> ordering in next-nearest-neighbor positions driven by Coulomb interactions and lattice-strain minimization. These results have important implications for both fundamental studies and applications of doped and alloyed metal-halide perovskites.

#### ■ INTRODUCTION

The facile synthesis, efficient and widely tunable luminescence, 1,2 and high defect tolerance of cesium-lead-halide perovskite (CsPbX<sub>3</sub>, X = Cl, Br, I) nanocrystals (NCs) have made these materials attractive for application in light-emitting diodes, 4-6 photovoltaics, 7,8 photodetectors, 9,10 and other optoelectronic technologies. The luminescence of CsPbX<sub>3</sub> NCs is easily tuned via postsynthetic anion exchange 11,12 and has also been modified by deliberate introduction of impurities, for example, divalent manganese<sup>6,13-16</sup> or trivalent lanthanides. 16-18 Among these materials, Mn2+-doped perovskite NCs have attracted particular attention for both their fundamental properties and for potential lighting and energy-conversion applications.  $^{6,13-16,19-22}_{}$  Mn<sup>2+</sup>:CsPb(Cl<sub>1-x</sub>Br<sub>x</sub>)<sub>3</sub> NCs usually show the coexistence of sharp, compositiontunable excitonic emission with broad, orange  $\mathrm{Mn}^{2+}$   $^4\mathrm{T}_{1g} \to$  ${}^{6}A_{1g} d-d$  emission, providing the ability to generate white light.

Although Mn<sup>2+</sup> is readily doped into CsPbCl<sub>3</sub> NCs, it has proven surprisingly challenging to dope Mn<sup>2+</sup> into CsPbBr<sub>3</sub> NCs directly. 6,23 Similarly, Mn<sup>2+</sup> is readily inserted into CsPbCl<sub>3</sub> NCs by postsynthetic partial cation exchange, <sup>16,24,25</sup> but the same approach has not been fruitful for doping Mn<sup>2+</sup> into CsPbBr<sub>3</sub> NCs. Mn<sup>2+</sup>-doped CsPb(Cl<sub>1-x</sub>Br<sub>x</sub>)<sub>3</sub> NCs (0 < x $\leq$  1) can be accessed by postsynthetic Cl<sup>-</sup>  $\rightarrow$  Br<sup>-</sup> anion exchange starting from preformed Mn2+:CsPbCl3 NCs, and this approach additionally allows the PL of a given ensemble of NCs to be tracked as a function of x. Such studies have revealed an unusual trend of increasing excitonic PL intensities and decreasing Mn<sup>2+</sup> d-d PL intensities with increasing Br content. 6,26-28 Compositional analysis before and after anion exchange argues against Mn2+ loss as the main cause of the decreasing Mn<sup>2+</sup> luminescence following anion exchange, <sup>20</sup> and instead, more complex photophysical phenomena such as thermally assisted Mn<sup>2+</sup> → exciton back energy transfer at high Br content (narrow exciton-Mn<sup>2+</sup>(<sup>4</sup>T<sub>1g</sub>) energy gap) have been implicated.<sup>6,26</sup>

A common postulation in discussions of anion exchange in metal-halide perovskites is that the cation sublattice is

Received: July 3, 2019 Revised: August 16, 2019 Published: August 19, 2019

Department of Chemistry, University of Washington, Seattle, Washington 98195, United States

<sup>\*</sup>Department of Physics, University of Washington, Seattle, Washington 98195, United States

<sup>§</sup>Department of Electrical and Computer Engineering, University of Washington, Seattle, Washington 98195, United States

effectively rigid and remains intact.<sup>6,11,29</sup> Given the ease of Mn<sup>2+</sup> (or other cation) insertion into CsPbCl<sub>3</sub> NCs by cation exchange or diffusion doping, <sup>15,16,30,31</sup> however, it appears likely that both cations and anions may migrate within the NCs during anion exchange. Pb2+ migration may be undetectable in undoped perovskites, but in Mn<sup>2+</sup>-doped CsPbX<sub>3</sub> perovskites, cation migration during anion exchange could potentially generate detectable nonrandom Pb2+ and Mn2+ spatial distributions. Spinodal decomposition has already been reported in CsPbCl<sub>3</sub> nanoplatelets at high Mn<sup>2+</sup> content (>6%) under solvothermal diffusion-doping conditions (80 mol % Mn to Pb, autoclave, 200 °C for 2-5 h), 32 forming what appear to be CsMnCl<sub>3</sub> inclusions within the CsPbCl<sub>3</sub> lattice. On the other hand, solid-state 133Cs nuclear magnetic resonance (NMR) spectroscopy has been used to rule out the formation of even small (radius  $\geq \sim 2.2$  nm ( $\sim 3$  unit cells)) CsMnCl<sub>3</sub> inclusions in bulk 3% Mn<sup>2+</sup>:CsPbX<sub>3</sub> (X = Cl or Br) powders, but the possibility of smaller clusters could not be addressed.<sup>33</sup> Neither of these studies examined mixed-halide compositions. The effect of anion exchange on Mn<sup>2+</sup> dopants within metal-halide perovskite NCs has not yet been examined.

Here, we use X-band electron paramagnetic resonance (EPR) and PL spectroscopies to track Mn<sup>2+</sup> ions during the postsynthetic transformation of Mn<sup>2+</sup>-doped CsPbCl<sub>3</sub> NCs into  $Mn^{2+}$ -doped CsPb( $Cl_{1-x}Br_x$ )<sub>3</sub> (0 <  $x \le 1$ ) NCs by roomtemperature anion exchange. These experiments reveal that Mn<sup>2+</sup> ions do indeed migrate within the NCs, clustering together in nearest-neighbor positions as Cl<sup>-</sup> is replaced by Br in the lattice. Density functional theory (DFT)-based Monte Carlo modeling predicts such Mn<sup>2+</sup> clustering, driven by differential Mn-X bond strengths. Even in the Mn<sup>2+</sup>:CsPbCl<sub>3</sub> and Mn<sup>2+</sup>:CsPbBr<sub>3</sub> composition limits, the modeling predicts spinodal decomposition to form domains of a new ordered phase with second-nearest-neighbor Mn<sup>2+</sup>-Mn2+ correlations, rather than the randomly doped Mn<sup>2+</sup>:CsPbX<sub>3</sub> typically assumed. This spinodal decomposition is driven by Coulomb effects and lattice-strain minimization. Overall, these combined experimental and modeling results highlight the structural richness and complexity of alloyed metal-halide perovskites. In particular, the observation of anion-dependent B-site cation distributions has important ramifications for the interpretation of the physical properties displayed by doped or alloyed perovskite NCs and for harnessing those properties in next-generation photonics applications.

## ■ METHODS

**Chemicals.** Unless otherwise stated, all chemicals were used as purchased without further purification. Lead(II) acetate trihydrate (99.9%) was purchased from Baker. Cesium acetate (99.9%), cesium bromide (99.9%), manganese(II) bromide hydrate (98%), and lead bromide (99.98+%) were purchased from Alfa Aesar. Manganese(II) acetate tetrahydrate (99.999%) was purchased from Strem. Oleylamine (70%, technical grade), oleic acid (90%, technical grade), trimethylsilyl bromide (97%), trimethylsilyl chloride (99%), boron nitride, and 3-methylpentane (99%, further dried over sodium benzophenone and distilled before use) were purchased from Sigma-Aldrich. Anhydrous toluene was purified through an alumina column pressurized with Ar. Mn(oleate)<sub>2</sub> was synthesized according to a literature procedure.<sup>34</sup> Hydrochloric acid (ACS plus), ethyl acetate (ACS), and acetone (ACS) were purchased from Fisher Chemical.

Synthesis of Mn<sup>2+</sup>:CsPbCl<sub>3</sub> NCs and Undoped CsPbCl<sub>3</sub> NCs. The synthesis of Mn<sup>2+</sup>:CsPbCl<sub>3</sub> was adapted with a modification from

the literature. 15 Briefly, in a glovebox under dinitrogen atmosphere, 0.1 mmol of CsOAc was added to a scintillation vial followed by 5 mL of toluene. This step was performed under inert conditions because CsOAc is highly deliquescent. The vial was then removed from the glovebox, and 0.1 mmol of PbOAc<sub>2</sub>·3H<sub>2</sub>O, 0.005 mmol of MnOAc<sub>2</sub>· 4H<sub>2</sub>O, 100  $\mu$ L of oleylamine, and 450  $\mu$ L of oleic acid were added. The mixture was allowed to stir capped at RT for 30 min to completely solubilize the acetate salts. Concentrated HCl acid (100  $\mu$ L) was then injected while stirring, and the reaction was allowed to proceed for 1 min. After this step, the NC solution was transferred to centrifuge tubes and flocculated with the addition of anhydrous ethyl acetate, followed by centrifugation and resuspension with hexanes. This precipitation-centrifugation-suspension step was carried out an additional time to remove unreacted species. After these two washing steps, there was no further change in Mn<sup>2+</sup> concentration as measured by inductively coupled plasma-atomic emission spectroscopy. The final product was dried in vacuo, transferred to the glovebox, and resuspended in hexanes for further manipulation. The Mn<sup>2+</sup>:CsPbCl<sub>3</sub> NC samples prepared for these studies typically showed photoluminescence quantum yields (PLQYs) of  $\sim$ 40% for the Mn<sup>2+</sup> d-dtransition. Undoped CsPbCl<sub>3</sub> NCs were made similarly, with the omission of the MnOAc<sub>2</sub>·4H<sub>2</sub>O. The doped and undoped NCs were stored under inert atmosphere and did not show any noticeable degradation over the course of the study.

**Synthesis of 0.1% Mn<sup>2+</sup>:CsPbBr<sub>3</sub> Bulk Powder.** Bulk powders were synthesized by grinding the reactants in a planetary ball mill using a zirconia grinding jar and balls (Ø 30 mm) for 1 h at 600 rpm. The resulting powder is further annealed at 250 °C for 30 min. For the synthesis, 3 mmol of CsBr, 0.003 mmol of MnBr<sub>2</sub>·xH<sub>2</sub>O, and 2.997 mmol of PbBr<sub>2</sub> were used.

**General Anion Exchange.** A 0.1 M solution of TMS-Br in hexanes was prepared for use in anion-exchange reactions. In a general anion-exchange reaction, a specific amount of TMS-Br solution was titrated into a solution of CsPbCl $_3$  NCs. The mixture was allowed to react until there was no further change in the energy of the excitonic emission. Following complete reaction, the solution was removed in vacuo to remove the TMS-Cl byproduct, and the NCs were then resuspended for further measurements. The time delay between TMS-Br addition and EPR measurement was less than  $\sim$ 10 min.

**Reverse Anion Exchange.** In a general reverse-anion-exchange reaction, a solution of CsPbBr<sub>3</sub> NCs was dried to a powder and a specific amount of neat TMS-Cl was added. The NCs suspend in the TMS-Cl. The mixture was allowed to react until the desired exciton emission energy was reached. Following reaction, the solution was removed in vacuo to remove unreacted TMS-Cl and the TMS-Br byproduct, and the NCs were then resuspended in 3-methylpentane for further measurements.

General Characterization. UV-vis measurements were performed on an Agilent Cary 60 spectrophotometer. Samples were prepared for powder X-ray diffraction (XRD) by depositing NCs from solution onto a silicon substrate and analyzed on a Bruker D8 Discover diffractometer. TEM samples were prepared by drop casting suspensions of NCs onto 400 mesh carbon-coated copper grids from TED Pella, Inc. and dried under an inert atmosphere. TEM images were obtained on an FEI TECNAI G2 F20 microscope operated at 200 kV. Size distributions were determined by analysis of >200 individual NCs. Elemental composition was determined on nitricacid-digested samples using inductively coupled plasma-atomic emission spectroscopy (ICP-AES) with a PerkinElmer 8300 spectrometer. For EDS analysis, samples were drop cast onto silicon substrates and coated with an ~200 nm thick layer of carbon; spectra were acquired in an FEI Sirion Scanning Electron Microscope operating at 30 kV using an Oxford EDS spectrometer. Standardless quantification was used. PLQY measurements were performed according to procedures described previously.

EPR Measurements. Continuous-wave electron paramagnetic resonance (EPR) measurements were performed on a Bruker EMX spectrometer operated at X-band frequencies equipped with an  $\rm LN_2$  variable-temperature sample-cooling unit.

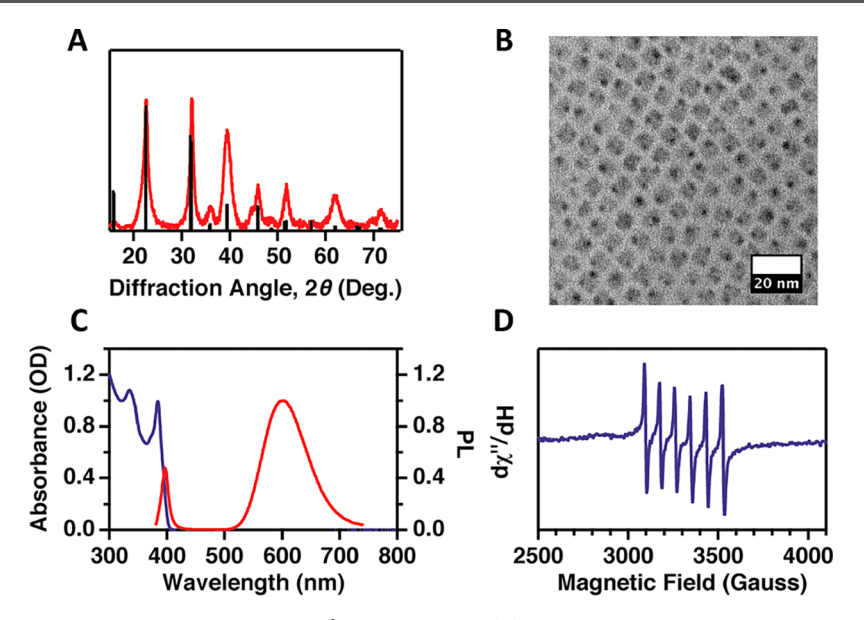


Figure 1. Characterization of representative colloidal 1.1% Mn<sup>2+</sup>:CsPbCl<sub>3</sub> NCs. (A) Powder X-ray diffraction data collected for Mn<sup>2+</sup>:CsPbCl<sub>3</sub> NCs drop-cast on a silicon substrate (red) and literature pattern (black) for orthorhombic CsPbCl<sub>3</sub> NCs. The NC data are consistent with the literature pattern. (B) TEM image of Mn<sup>2+</sup>:CsPbCl<sub>3</sub> NCs, with the scale bar representing 20 nm. The average edge length is  $6.9 \pm 0.4$  nm. (C) Absorption (blue) and photoluminescence (red) spectra of the Mn<sup>2+</sup>:CsPbCl<sub>3</sub> NCs. A 365 nm diode was used for photoexcitation. (D) X-band electron paramagnetic resonance (EPR) spectrum of the Mn<sup>2+</sup>:CsPbCl<sub>3</sub> NCs. All data were collected at room temperature.

<sup>133</sup>Cs Solid-State NMR Measurements. Solid-state MAS NMR spectra of  $^{133}$ Cs (91.8 MHz at 16.5 T) were recorded on a Bruker Avance III 16.5 T spectrometer equipped with a 3.2 mm Phoenix HXY probe. NC samples were dried and mixed with boron nitride forming a powder suitable for packing. The powders were then packed into 3.2 mm zirconia rotors and closed using Vespel caps. The samples were spun at 3 kHz MAS using dry air, and the temperature was maintained at 298 K.  $^{133}$ Cs shifts were referenced to solid CsCl ( $\delta$  = 223.2 ppm).  $^{35}$  Relaxation delays ranged from 6 to 10 min depending on the samples. The saturation-recovery experiments were performed by applying a train of 30  $\pi$ /2 pulses spaced by 3 ms in keeping with a previous report.  $^{33}$  For analysis and discussion of these results, see Figure S16 and Table S1.

Photoluminescence Measurements. Room-temperature photoluminescence measurements were performed on solutions of NCs excited with a 365 nm LED or a 375 or 405 nm laser diode and collected with an OceanOptics USB 2000+ spectrometer or an LN<sub>2</sub>-cooled charge-coupled device (CCD) mounted to a monochromator. Spectra are corrected for the instrument response. Liquid helium photoluminescence experiments were performed on films of NCs sandwiched between quartz plates. Samples were mounted in a flow cryostat with a variable-temperature sample compartment.

For lifetime measurements, photoexcitation was provided by a 375 or 405 nm laser diode modulated using the square pulse waveform output of a function generator at a 10 Hz repetition rate. The PL was coupled into a fiber and passed to a monochromator equipped with LN<sub>2</sub>-cooled CCD and photomultiplier tube (PMT) detectors. Photoluminescence decay kinetics were measured using a multichannel scaler, averaging over several thousand laser pulses.

**Modeling.** Characterization of the space of low-energy alloy configurations on the Pb- and halide-sublattices at the level of first-principles theory is limited by the computational demands introduced by the alloy degrees of freedom. For instance, a fixed lattice of n Pb sites and 3n halide sites admits  $2^{4n}$  possible configurations of Pb/Mn and halide, and determining the ab initio ground-state energy of each configuration requires optimization of both electronic and ionic degrees of freedom. While the number of configurations could be reduced by equivalence under symmetry operations from the space group of the underlying lattice, the number of structural calculations required to sufficiently sample the configuration space is still at best computationally inefficient and at worst infeasible.  $^{36}$ 

To reduce the computational complexity of the problem, we built a model for the bulk energetics of halide mixing in the presence of substitutional Mn<sup>2+</sup> using the cluster expansion (CE) formalism.<sup>37</sup> To elaborate, the configuration of various chemical components on a lattice of N sites can be represented by a vector  $\boldsymbol{\sigma}=(\sigma_1,\sigma_2,...,\sigma_N)$ , where if  $M_i$  chemical components can occupy lattice site i, then admissible values of the site occupation variable  $\sigma_i$  are  $\sigma_i \in \{0, 1, ..., M_i-1\}$ . Similarly, a cluster of sites can be represented by a vector  $\boldsymbol{\alpha}=(\alpha_1,\alpha_2,...,\alpha_N)$  that spans all sites in the lattice, where  $\sigma_i=0$  if site i is not in the cluster and  $\sigma_i \in \{0, 1, ..., M_i-1\}$  otherwise. Then, orthogonal, single-site functions that faithfully represent the occupation of lattice sites in a cluster can be defined in the basis of Chebyshev polynomials:

$$\phi_{\alpha_{i},M_{i}}(\sigma_{i}) = \begin{cases} 1 & \text{if } \alpha_{i} = 0 \\ -\cos\left(2\pi \left\lceil \frac{\alpha_{i}}{2} \right\rceil \frac{\sigma_{i}}{M_{i}}\right) & \text{if } \alpha_{i} > 0 \text{ and odd} \end{cases}$$

$$-\sin\left(2\pi \left\lceil \frac{\alpha_{i}}{2} \right\rceil \frac{\sigma_{i}}{M_{i}}\right) & \text{if } \alpha_{i} > 0 \text{ and even} \end{cases}$$

$$(1)$$

Here, [...] in eq 1 denotes the ceiling function.<sup>38</sup> The ground-state energy,  $E(\sigma)$ , of a given configuration of alloyed species can be expanded in a complete, orthonormal, basis of cluster functions as  $E(\sigma) = E_0 + \sum_{\alpha} J_{\alpha} g_{\alpha} \overline{\Gamma}_{\alpha}(\sigma)$ , where the cluster function  $\Gamma_{\alpha}(\sigma) = \Pi_i \phi_{\alpha_{\nu} M_i}(\sigma_i)$  is a product of single-site functions in cluster  $\alpha$  and the  $\overline{\Gamma}_{\alpha}$  denotes an average over clusters equivalent under symmetry operations of the underlying lattice. Hence, the sum in the expansion is carried out over symmetrically distinct clusters, and each cluster carries a multiplicity factor  $g_{\alpha}$ . The coefficients of the expansion  $J_{\alpha}$  are commonly called effective cluster interactions (ECIs) and constitute a coarse-grained description of the underlying electronic and ionic degrees of freedom that contribute to the ground-state energy of a configuration. Once the ECIs have been determined, the energy of any configuration on the lattice can be rapidly calculated.

The ECIs were determined from density functional theory (DFT) calculations of the energies of 200 distinct structures. To enhance model sparsity and optimize bias-variance trade-off, cluster selection and ECI fitting were carried out using a Least Absolute Shrinkage and Selection Operator (LASSO) regression combined with 10-fold cross-

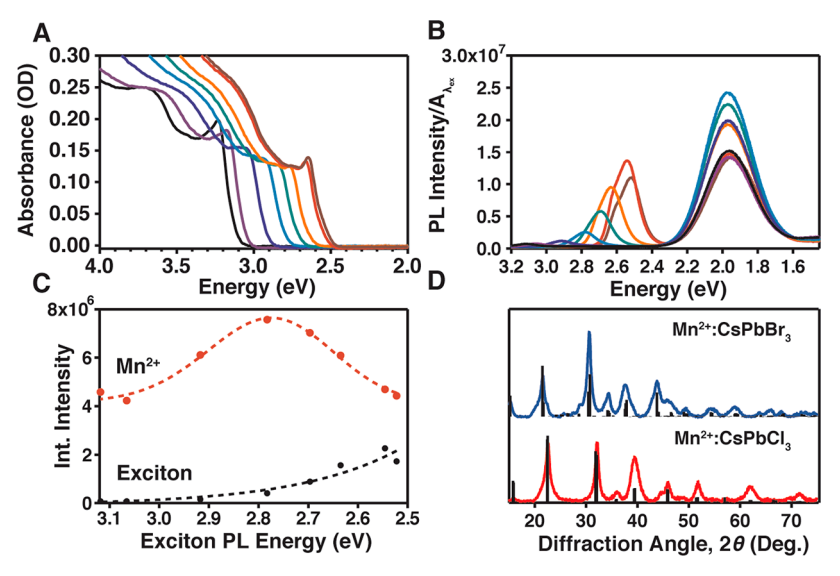


Figure 2. (A) UV—vis absorption spectra of  $1.1\% \, \mathrm{Mn^{2+}}$ : CsPbCl $_3$  NCs collected during the course of an anion exchange reaction using trimethylsilyl bromide (TMS-Br). (B) Corresponding PL spectra collected during the course of anion exchange. NCs were photoexcited at 375 nm. The PL spectra are plotted relative to the optical density of the sample at the excitation wavelength, allowing relative changes in quantum yield during anion exchange to be assessed. (C) Total integrated excitonic (black) and  $\mathrm{Mn^{2+}} \, d - d$  (orange) PL intensities from the data in panel B, plotted against the energy of the excitonic PL. The dashed lines are guides to the eye. (D) Powder X-ray diffraction data collected before and after anion exchange. Both patterns are consistent with the orthorhombic phase.

validation to determine the regularization parameter.<sup>39</sup> The CE model was found to have a root-mean squared error (RMSE) of ~2 meV/ atom. Monte Carlo (MC) simulations using the CE energy model and the Metropolis-Hastings algorithm with Kawasaki exchange were used to sample room-temperature, equilibrium alloy configurations in the canonical ensemble for various fixed Pb/Mn and Cl/Br compositions. Each MC run was initialized with a random configuration of alloy components, and a minimum of 1000 MC passes were performed to statistically sample the energy and short-range order observables, as discussed in the Results and Analysis. Each MC pass is defined as the number of MC trials becomes equal to the number of alloyed sites in the simulation cell, where each simulation cell consisted of 32 000 alloyed sites. The CASM software and Scikit-learn libraries were used in automating the first-principles calculations, developing the cluster expansion, and performing MC.<sup>40–45</sup>

DFT calculations based on the all-electron projector-augmented wave (PAW) method were performed using the Vienna Ab Initio Simulation Package (VASP). 46-50 The conjugate gradient algorithm was used for structural optimization, and the volume, shape, and atomic positions were relaxed until interatomic Hellmann-Feynman forces were less than 0.01 eV/Å. To reduce total computation time, the structure was optimized using the Perdew-Burke-Ernzerhof (PBE) exchange-correlation functional in the generalized gradient approximation (GGA).<sup>51</sup> In the pseudopotentials, 9 electrons of Cs  $(5s^25p^66s^1)$ , 4 electrons of Pb  $(6s^26p^2)$ , 7 electrons of Cl  $(3s^23p^5)$ , 7 electrons of Br (4s<sup>2</sup>4p<sup>5</sup>), and 7 electrons of Mn (3d<sup>5</sup>4s<sup>2</sup>) were treated as valence electrons. The plane-wave basis cutoff was set to 520 eV, and a Gamma-centered Monkhorst Pack k-point mesh was used for Brillouin-zone integration. 52 A k-point density of 5000 k-points per reciprocal number of atoms, which amounts to a  $10 \times 10 \times 10$  k-point mesh for a 5-atom, cubic unit cell, was found to be well-converged for various simulation cell sizes.

# **■ RESULTS AND ANALYSIS**

**Synthesis and General Characterization.** Figure 1 plots general characterization data for a representative sample of assynthesized Mn<sup>2+</sup>:CsPbCl<sub>3</sub> NCs. The average concentration of Mn<sup>2+</sup> in this sample is 1.1%, as determined by ICP-AES. Figure 1A plots powder-X-ray diffraction data for this sample. The NC data index well to the pattern for orthorhombic CsPbCl<sub>3</sub>,

and no additional phases are observed. Figure 1B shows a representative TEM image of these NCs. The NCs are approximately cubic in shape with good size homogeneity and an average particle edge length of 6.9  $\pm$  0.4 nm. Figure 1C plots room-temperature absorption and PL spectra of these NCs. The absorption spectrum shows a sharp first-exciton band centered at 395 nm, and the PL spectrum shows narrow excitonic PL at 400 nm as well as an intense, broad band centered at 610 nm assigned as the  ${}^4T_{1g} \rightarrow {}^6A_{1g}$  ligand-field transition of octahedral Mn<sup>2+</sup>. Figure 1D plots the roomtemperature X-band EPR spectrum of these Mn<sup>2+</sup>:CsPbCl<sub>3</sub> NCs. This spectrum shows a resonance at g = 2.01, split into six lines by hyperfine coupling with the Mn<sup>2+</sup> nuclear spin. From this splitting, a hyperfine coupling constant of 80.9  $\times$ 10<sup>-4</sup> cm<sup>-1</sup> is obtained, consistent with previous reports. <sup>13,53</sup> As noted previously, this hyperfine splitting is very large compared to those of Mn<sup>2+</sup>-doped chalcogenide II-VI semiconductor NCs, reflecting the high ionicity of Mn<sup>2+</sup> bonding in the CsPbCl<sub>3</sub> lattice.<sup>54</sup>

**General Anion-Exchange Reactions.** Trimethylsilyl halides (TMS-X, X = Cl, Br, I) have been demonstrated to be useful anion-exchange reagents in elpasolite (double-perovskite) NCs<sup>55</sup> and CsPb $X_3$  NCs and thin films. <sup>56</sup> Here, we apply TMS-Br to induce anion exchange in Mn<sup>2+</sup>:CsPbCl<sub>3</sub> perovskite NCs. Figure 2 summarizes the evolution of Mn<sup>2+</sup>:CsPb $X_3$  NC physical characteristics during this anion exchange. Figure 2A shows that the first absorption maximum shifts to lower energy with added TMS-Br, consistent with Cl $\rightarrow$  Br $^-$  anion exchange. At the end point of the reaction (excess TMS-Br), SEM/EDX measurements confirm essentially complete halide exchange with no significant change in Mn<sup>2+</sup> content (see Figure S1).

Figure 2B plots PL spectra collected as a function of added TMS-Br. These data also show a red-shift of the excitonic emission with added bromide, but there is no clear change in the energy of the  $Mn^{2+}$  d-d emission. A blue shoulder in the excitonic region appears with greater bromide incorporation,

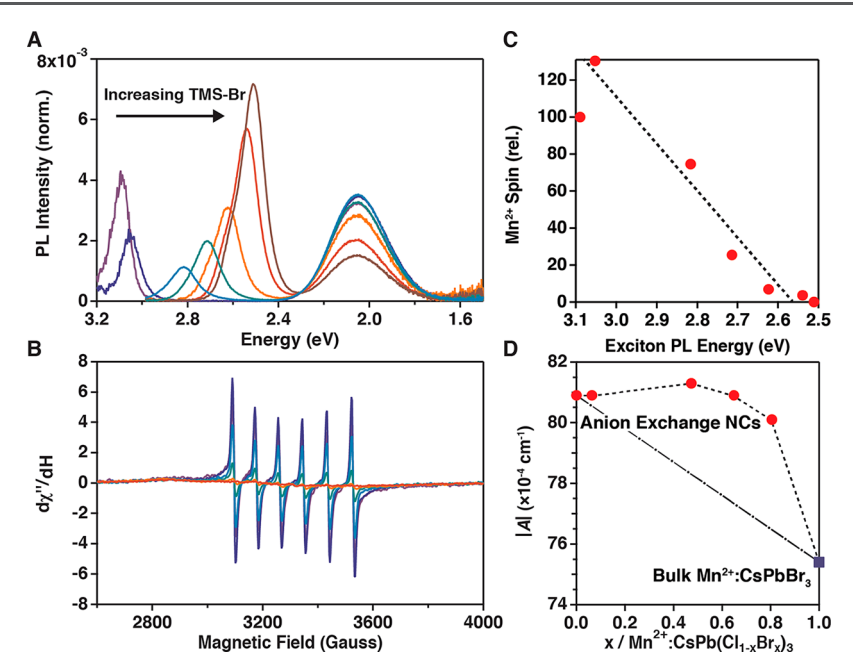


Figure 3. (A) PL spectra of 1.1%  $Mn^{2+}$ :CsPbCl<sub>3</sub> NCs in the EPR tube during the course of an anion exchange reaction; note that  $Mn^{2+}$  PL is seen centered at ~610 nm at every stage of the anion exchange reaction. The PL spectra are each normalized to their total integrated PL intensity. A 365 nm diode was used for excitation. Each spectrum was taken at the same NC concentration, and the NCs were never removed from the EPR tube over the entire experiment. (B) X-band EPR spectra collected during the course of the same anion exchange reaction as described in panel A. (C) Scatter plot of the relative  $Mn^{2+}$  spin, determined from double integration of the EPR spectra, vs the exciton PL peak energy from (A). The dashed line is a guide to the eye. (D) Summary of hyperfine splitting constants, |A|, for  $Mn^{2+}$ :CsPb( $Cl_{1-x}Br_x$ )<sub>3</sub> NCs measured during anion exchange, taken from the spectra collected in (B) and for  $Mn^{2+}$ :CsPbBr<sub>3</sub> bulk powder taken from the spectrum in Figure S6. The dashed line (- · -) is a guide to the eye, tracing the experimental hyperfine splitting constants. The dot-dashed line (- · -) illustrates the  $Mn^{2+}$  hyperfine splittings expected for random solid solutions of halides in CsPbX<sub>3</sub>. Bromide concentrations are estimated from the known dependence of the excitonic PL energy on x.

attributed to sample inhomogeneity. These PL spectra have been corrected for the optical density of the sample at the excitation wavelength, allowing quantitative analysis of their integrated intensities (i.e., relative PL quantum yields) over the course of the anion-exchange reaction, and these intensities are summarized in Figure 2C. The same PL spectra normalized to their total integrated intensities (which corrects for changes in PL quantum yield) or normalized to the exciton maxima (for comparison with published data<sup>6,57</sup>) are provided in Figure S2. From Figure 2C, the excitonic PL becomes much brighter as Br<sup>-</sup> is incorporated, whereas the Mn<sup>2+</sup> PL intensity first grows but then decreases with increasing Br incorporation. These trends are generally consistent with previous data<sup>6,26</sup> but show substantially more Mn<sup>2+</sup> PL from the resulting Mn<sup>2+</sup>:CsPbBr<sub>3</sub> NCs than observed in other samples. Overall, these data demonstrate that Mn2+ PL is still sensitized by NC photoexcitation even after complete Cl<sup>-</sup> → Br<sup>-</sup> anion exchange. Figure 2D plots powder X-ray diffraction data collected before and after NC anion exchange. The orthorhombic crystal structure of the parent Mn<sup>2+</sup>:CsPbCl<sub>3</sub> NCs is preserved upon conversion to Mn<sup>2+</sup>:CsPbBr<sub>3</sub>.

According to previous literature, the changes in  $\mathrm{Mn^{2^+}}$  and exciton PL intensities with anion exchange (Figure 2C) can be attributed to two effects. First, the increase in both the excitonic and  $\mathrm{Mn^{2^+}}$  PL intensities with initial Br<sup>-</sup> incorporation is consistent with observations made for analogous undoped NCs; the exciton PL quantum yield in undoped CsPbCl<sub>3</sub> NCs generally increases substantially with  $\mathrm{Cl^-} \to \mathrm{Br^-}$  anion exchange, 11,12 because narrowing the perovskite energy gap diminishes nonradiative recombination losses by reducing the number of accessible surface traps. Second, the decrease in  $\mathrm{Mn^{2^+}}$  PL intensity at larger Br<sup>-</sup> content and the corresponding

increase in excitonic PL intensity could reflect thermally assisted "back" energy transfer from Mn<sup>2+</sup> to repopulate the excitonic excited state when their energy difference narrows sufficiently.<sup>6,26</sup> It is conceivable that such back energy transfer does occur in  $Mn^{2+}$ : CsPb(Cl<sub>1-x</sub>Br<sub>x</sub>)<sub>3</sub> NCs with large x, but as noted previously,<sup>26</sup> this system is vastly different from the wellstudied system of dual-emitting II-VI Mn<sup>2+</sup>-doped NCs. 59,60 For example, in dual-emitting II-VI Mn<sup>2+</sup>-doped NCs, forward energy transfer is fast and thermally assisted back energy transfer is strongly suppressed when the temperature is lowered, yielding almost exclusively Mn<sup>2+</sup> PL at low temperatures; however, the PL of Mn2+:CsPb(Cl<sub>0.22</sub>Br<sub>0.78</sub>)<sub>3</sub> NCs prepared here does not show an analogous temperature dependence (see Figures S8 and S9). Instead, the excitonic PL from these NCs increases and their Mn<sup>2+</sup> PL decreases with decreasing temperature before both turn over at ~75 K, and substantial excitonic PL is still observed even at 5 K. In fact, this temperature dependence appears very similar to the behavior reported for Mn<sup>2+</sup>:CsPbCl<sub>3</sub> NCs,<sup>54</sup> which have too large an energy gap for back energy transfer. These observations support the conclusion of a more complicated origin of the spectral changes in Mn<sup>2+</sup>:CsPb(Cl<sub>1-x</sub>Br<sub>x</sub>)<sub>3</sub> NCs with anion exchange. As detailed below, the experiments performed here identify a new and unrecognized complication contributing to such PL trends: Mn<sup>2+</sup> clustering within the NC lattice during anion exchange.

Evidence for Mn<sup>2+</sup> Clustering upon Anion Exchange. To probe Mn<sup>2+</sup> speciation, EPR measurements were also performed at various stages of anion exchange. For these measurements, anion exchange was performed in a gastight EPR tube, and both PL and EPR data were collected after addition of each TMS-Br aliquot. Importantly, the product of

the anion-exchange reaction is gaseous TMS-Cl, which can be removed without removing any NCs, and the solvent volume can be kept constant. Consequently, Mn<sup>2+</sup> cannot be lost from the EPR tube because the sample is never removed from the EPR tube throughout the entire experiment.

Figure 3A plots the PL spectra of a sample of Mn<sup>2+</sup>:CsPbCl<sub>3</sub> NCs collected during the course of such an anion-exchange reaction. Each spectrum corresponds to a different stage of TMS-Br titration. As in Figure 2C, TMS-Br addition redshifts the excitonic PL as the host lattice is converted from CsPbCl<sub>3</sub> to CsPbBr<sub>3</sub>, but the Mn<sup>2+</sup> d-d PL energy remains largely unchanged. In contrast with the data in Figure 2C, the spectra in Figure 3A have all been normalized to their total integrated areas because the optical density of the solution in the EPR tube was too high to measure accurately, so only trends in relative PL intensities can be interpreted. Nonetheless, the key observation from the PL data is that, as in Figure 2C, Mn<sup>2+</sup> PL is still sensitized by NC photoexcitation even after complete anion exchange, and hence, some if not all of the Mn<sup>2+</sup> is still intimately integrated with the NCs and likely still inside the NC lattice.

Figure 3B plots EPR spectra collected during this same anion-exchange reaction. A striking decrease in the Mn<sup>2+</sup> EPR intensity is observed as TMS-Br is added, and at maximum anion exchange, there is no detectable Mn<sup>2+</sup> EPR signal at all. Again, we stress that this loss of EPR intensity *cannot* be associated with any actual loss of Mn<sup>2+</sup> from the EPR tube. Figure 3C summarizes the change in double-integrated EPR intensity with anion exchange, the latter represented in terms of the excitonic PL energy. This result shows a strong correlation between the incorporation of Br<sup>-</sup> into the NCs and the loss of EPR-active Mn<sup>2+</sup>, despite the retention of Mn<sup>2+</sup> PL.

ICP-AES measurements confirm that Mn<sup>2+</sup> is still strongly associated with the perovskite NCs after anion exchange: The starting Mn<sup>2+</sup> concentration was measured to be 1.1% (of total B-site cations) in these NCs. After complete anion exchange and spectroscopic measurement, the NCs were removed from the EPR tube and washed twice by standard precipitation/ centrifugation/resuspension methods to eliminate any Mn<sup>2+</sup> that may have been expelled from the NCs, and the remaining NC sample was then analyzed by ICP-AES. The resulting Mn<sup>2+</sup> concentration was still 1%, i.e., within error of the starting concentration. The data thus rule out loss of Mn<sup>2+</sup> from the NCs. This conclusion is bolstered by the continued absence of any EPR signal even at 120 K; the EPR spectra of plausible solvated Mn<sup>2+</sup> species (e.g., Mn(oleate)<sub>2</sub>) are readily detectable at low temperatures (see Figures S3-S5). Moreover, this low-temperature result also indicates that the loss of Mn<sup>2+</sup> EPR intensity does not result from accelerated Mn<sup>2+</sup> spin relaxation in the CsPbBr<sub>3</sub> lattice. For reference, we prepared bulk 0.1% Mn<sup>2+</sup>:CsPbBr<sub>3</sub> and confirmed that its EPR signal is readily detectable at room temperature (see Figure S6).

Insight into this strange loss in  $\mathrm{Mn^{2+}}$  EPR intensity with anion exchange is obtained by analysis of the  $\mathrm{Mn^{2+}}$  hyperfine splittings observed in Figure 3B. These hyperfine splittings are summarized in Figure 3D. In the starting  $\mathrm{Mn^{2+}}$ :CsPbCl<sub>3</sub> NC EPR spectrum (Figure 3B), the hyperfine splitting constant is  $\mathrm{IAI} = 80.9 \times 10^{-4} \ \mathrm{cm^{-1}}$ , consistent with literature results. Interestingly, there is little or no detectable change in the hyperfine splitting constant over the entire course of the anion-exchange reaction. For comparison, the EPR spectrum of  $\mathrm{Mn^{2+}}$ :CsPbBr<sub>3</sub> shows a hyperfine splitting of  $\mathrm{IAI} = 75.4 \times 10^{-4} \ \mathrm{cm^{-1}}$  (see Figure S6), illustrating the trend of decreasing

hyperfine splitting with increasing metal—ligand covalency within the local  $[MnX_6]^{4-}$  cluster. These observations yield the surprising conclusion that essentially *all* EPR-active  $Mn^{2+}$  remains exclusively chloride-coordinated and that  $Mn^{2+}$  ions coordinated by bromide either are not present in these NCs or are no longer EPR active. In this vein, it is perhaps telling that the literature does not yet have any clear examples of EPR spectra of  $Mn^{2+}$  in CsPbBr3 NCs, and the few examples that have been reported  $^{16,53}$  show hyperfine splittings *greater* than that of  $Mn^{2+}$  in CsPbBr3, suggesting oxygenic  $Mn^{2+}$  coordination.

To explain the above observations, we hypothesize that Cl-→ Br anion exchange causes Mn<sup>2+</sup> clustering within the perovskite NCs. Because of the 180° M<sup>2+</sup>-X-M<sup>2+</sup> bond angle in this lattice, nearest-neighbor Mn<sup>2+</sup>-Mn<sup>2+</sup> superexchange coupling in such clusters would be antiferromagnetic; 63 hence, this Mn<sup>2+</sup> would be EPR silent, but it could still luminesce. We further hypothesize that this clustering is driven thermodynamically by a preference for Mn-Cl rather than Mn-Br bonding. For example, the bond dissociation energies of Mn-Cl (MnCl<sub>2</sub>) and Mn-Br (MnBr<sub>2</sub>) are 392.5 and 332.2 kJ/mol,<sup>65</sup> respectively, reflecting this preference. To test this interpretation, we investigated whether the spectroscopic changes in Figure 3 are reversible, i.e., whether  $Br^- \rightarrow Cl^$ anion exchange could reintroduce a Mn<sup>2+</sup> EPR signal. For this experiment, we first converted 3.7% Mn<sup>2+</sup>:CsPbCl<sub>3</sub> NCs to Mn<sup>2+</sup>:CsPbBr<sub>3</sub> NCs as in Figure 3. Following conversion, these NCs were removed from the EPR tube and washed twice by standard precipitation/centrifugation/resuspension methods to eliminate any Mn<sup>2+</sup> that may have been ejected from the NCs. We then added neat TMS-Cl to the solution to drive the reverse anion exchange, again monitoring the PL and EPR. This reaction was performed under conditions that were otherwise identical to those used for Figure 3. In particular, the NCs were again not removed from the EPR tube during the  $Br^- \rightarrow Cl^-$  reverse anion exchange, and the NC concentration in the EPR tube was held constant. Figure 4A plots the evolution of the PL spectra during this reverse anion exchange. The excitonic PL shifts to higher energy, consistent with chloride incorporation, and concomitantly, the relative Mn<sup>2+</sup> PL intensity increases. The PL spectrum obtained after the full forward and reverse anion-exchange cycle is very similar to the initial spectrum, again consistent with full retention of Mn<sup>2+</sup> in the NCs. Figure 4B plots the corresponding EPR spectra. In this sample, anion exchange to form Mn<sup>2+</sup>:CsPbBr<sub>3</sub> NCs eliminates most but not all of the Mn<sup>2+</sup> EPR signal; the remaining EPR signal is weak, and its hyperfine splittings are unresolved. This breadth is consistent with Mn<sup>2+</sup> being magnetically concentrated, as hypothesized above. Upon reverse anion exchange, the EPR intensity increases again and hyperfine splittings emerge, consistent with dissociation of Mn<sup>2+</sup> clusters and randomization of the Mn<sup>2+</sup> spatial distribution. This recovered hyperfine splitting is described by  $|A| = 80.9 \times 10^{-4} \text{ cm}^{-1}$ , consistent with  $[\text{MnCl}_6]^{4-}$ . From these results, we conclude that  $Br^- \rightarrow Cl^-$  reverse anion exchange breaks up antiferromagnetic Mn2+ clusters formed during the  $Cl^- \rightarrow Br^-$  forward anion exchange.

Effects of  $\mathrm{Mn^{2+}}$  clustering are also observed by PL. Figure 5 summarizes  $\mathrm{Mn^{2+}}$  PL data collected at 5.2 K for 1.1%  $\mathrm{Mn^{2+}}$ :CsPbCl<sub>3</sub> NCs and for the same  $\mathrm{Mn^{2+}}$ :CsPb(Cl<sub>1-x</sub>Br<sub>x</sub>)<sub>3</sub> NCs after partial bromide exchange (x = 0.78). The main panel plots  $\mathrm{Mn^{2+}}$  PL decay curves for the two samples, and the corresponding 5.2 K PL spectra are shown in the inset. The

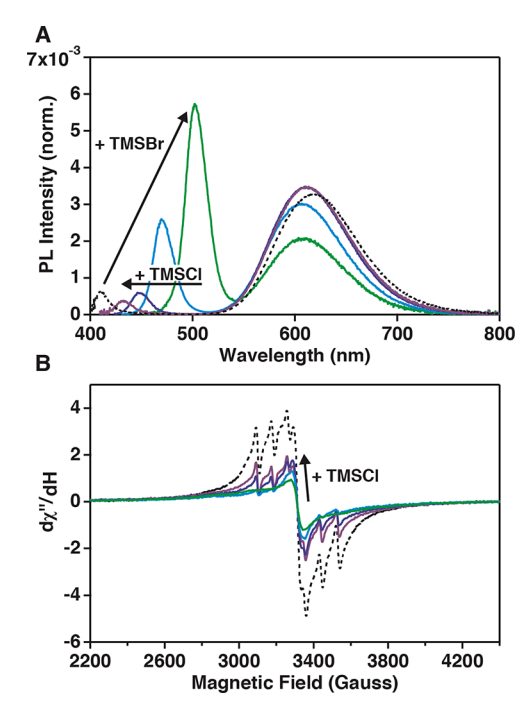


**Figure 4.** (A) Photoluminescence (PL) spectra of 3.7%  $\rm Mn^{2+}$ :CsPbBr<sub>3</sub> NCs collected during the course of reverse anion exchange. Mn<sup>2+</sup> PL at ~610 nm is observed at each stage of anion exchange. The PL spectra are normalized to the total integrated PL intensity. (B) Corresponding X-band EPR spectra of Mn<sup>2+</sup>:CsPbBr<sub>3</sub> NCs made via anion exchange of Mn<sup>2+</sup>:CsPbCl<sub>3</sub> NCs with TMS-Br during the course of a reverse anion exchange reaction using TMS-Cl. Each spectrum is taken at the same NC and Mn<sup>2+</sup> concentration, as in the experiment of Figure 3. The Mn<sup>2+</sup> hyperfine splitting constant is  $\rm IAI = 80.9 \times 10^{-4}~cm^{-1}$ . The broad feature underneath the sharper Mn<sup>2+</sup> hyperfine lines is assigned to magnetically concentrated Mn<sup>2+</sup>. EPR and PL spectra of the initial Mn<sup>2+</sup>:CsPbCl<sub>3</sub> NCs are shown as dashed lines.

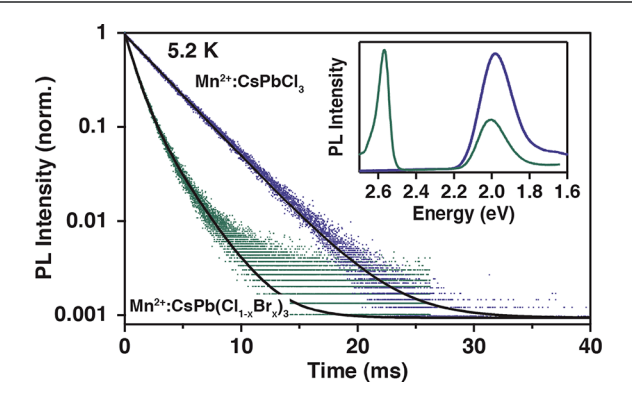


**Figure 5.** Photoluminescence decay curves measured for 1.1%  $\rm Mn^{2+}:CsPbCl_3$  NCs (blue) using 375 nm and for 1.1%  $\rm Mn^{2+}:CsPb-(Cl_{1-x}Br_x)_3$  NCs (x=0.78) (green) using 405 nm excitation. Both excitation sources were pulsed as square waves at a 10 Hz repetition rate. The data are normalized at time zero. Black lines are fits to the data. The data for the  $\rm Mn^{2+}:CsPbCl_3$  NCs are fit to a single-exponential function with a time constant of 3.36 ms. The data for the  $\rm Mn^{2+}:CsPb(Cl_{1-x}Br_x)_3$  NCs are fit to a double-exponential function with time constants of 859  $\mu s$  and 2.3 ms. The inset shows the corresponding PL spectra of the  $\rm Mn^{2+}:CsPbCl_3$  (blue) and  $\rm Mn^{2+}:CsPb(Cl_{1-x}Br_x)_3$  (green) NCs excited with 405 nm. All data were collected at 5.2 K. EPR spectra of these samples are shown in Figure 3. RT absorption spectra of these samples are provided in Figure S7.

Mn<sup>2+</sup>:CsPbCl<sub>3</sub> NCs show monoexponential PL decay with a lifetime of 3.4 ms, consistent with the spin- and parityforbidden  $Mn^{2+}$   $^4T_{1g} \rightarrow ^6A_{1g}$  ligand-field origin of this emission.  $^{54}$  In contrast, the  $Mn^{2+}$ :CsPb $(Cl_{1-x}Br_x)_3$  NCs show biexponential PL decay with components of 859  $\mu$ s and 2.3 ms. We note that the Mn<sup>2+</sup> PLQY increases after this anion exchange, possibly due to reduced exciton trapping prior to energy capture by Mn<sup>2+</sup>. Shorter Mn<sup>2+</sup> PL lifetimes are typically observed in bromide compared to chloride lattices (e.g., 54.9 ms in CsCaCl<sub>3</sub> vs 23 ms in CsMgBr<sub>3</sub>, respectively, at 10 K<sup>66,67</sup>), attributable to the increased spin-orbit coupling of the heavier halides, but this effect cannot explain the biexponential decay or the short time constant observed in Figure 5. Moreover, the hyperfine splittings in the EPR spectra of these NCs (Figure 3) indicate that Mn<sup>2+</sup> remains essentially exclusively coordinated by chloride anions, also ruling out an effect from bromide spin-orbit coupling. Mn2+ lifetime shortening due to thermal back energy transfer to the exciton state does not occur at these low temperatures either. Instead, we propose that this lifetime shortening is attributable to Mn<sup>2+</sup> clustering. In Mn<sup>2+</sup>-Mn<sup>2+</sup> dimers and other clusters, magnetic superexchange coupling generates spin ladders in both the ground and excited states that introduce new spin-allowed components to otherwise spin-forbidden electronic transitions, accelerating radiative decay. 68,69 High Mn<sup>2+</sup> concentrations also facilitate energy migration to traps, accelerating nonradiative decay. Collectively, the experimental results point to Mn<sup>2+</sup> migration and clustering induced by Cl<sup>−</sup> → Br<sup>−</sup> anion exchange in Mn<sup>2+</sup>:CsPb(Cl<sub>1-x</sub>Br<sub>x</sub>)<sub>3</sub> NCs.

Thermodynamics of  $Mn^{2+}$  Clustering. To explore the thermodynamics of  $Mn^{2+}$  clustering, we modeled atom distributions in  $Mn^{2+}$ :CsPb( $Cl_{1-x}Br_x$ )<sub>3</sub> using a cluster-expansion energy model and canonical Monte Carlo (MC) methods, as detailed in the Methods. Figure 6 shows energy-minimized distributions of  $Mn^{2+}$ ,  $Cl^-$ , and  $Br^-$  ions calculated for x = 0.80 and 1.00. Similar plots for the complete halide composition series are provided in Figure S10. A representative energy-minimization trajectory is also given in Figure S11.

We quantify clustering predicted by the MC simulations in terms of Warren-Cowley type short-range order (SRO) parameters given by eq 2,

$$\eta_i^{(\alpha|\beta)} = \frac{\langle p_i(\alpha|\beta) \rangle - c_\alpha}{1 - c_\alpha} \tag{2}$$

where  $p_i(\alpha|\beta)$  is the conditional probability that any  $\alpha$  species has a  $\beta$  species at a lattice distance  $i \in \{1NN, 2NN, 3NN, ...\}$ , and iNN is the ith nearest neighbor shell. 70 Because we do not consider anti-site formation in this work, in the case where  $\alpha =$  $\beta$ , iNN denotes the ith nearest neighbor shell on the  $\alpha$ sublattice. The fractional composition of the alloy species  $\alpha$  is given by  $c_{\alpha}$ , and  $\langle ... \rangle$  denotes a thermal average with respect to the canonical ensemble. The SRO parameters measure the degree of pairwise  $\alpha - \beta$  clustering. For nonzero concentrations of species  $\alpha$  and  $\beta$ , the SRO parameters vanish identically for a completely disordered state, which in principle occurs only in the limit of infinite temperature. The lower bound for the SRO parameter is given by  $-c_{\alpha}/(1-c_{\alpha})$ . A value  $0<\eta_{i}^{(\alpha|\beta)}\leq 1$ indicates a tendency toward ion segregation, and conversely,  $-c_{\alpha}/(1-c_{\alpha}) \leq \eta_{i}^{(\alpha|\beta)} \leq 0$  indicates a tendency toward local mixing with species distinct from  $\beta$  at the *i*th nearest neighbor. Figure 7 plots Mn<sup>2+</sup>-Mn<sup>2+</sup> SRO parameters for first, second,

and third NN positions as a function of the halide composition

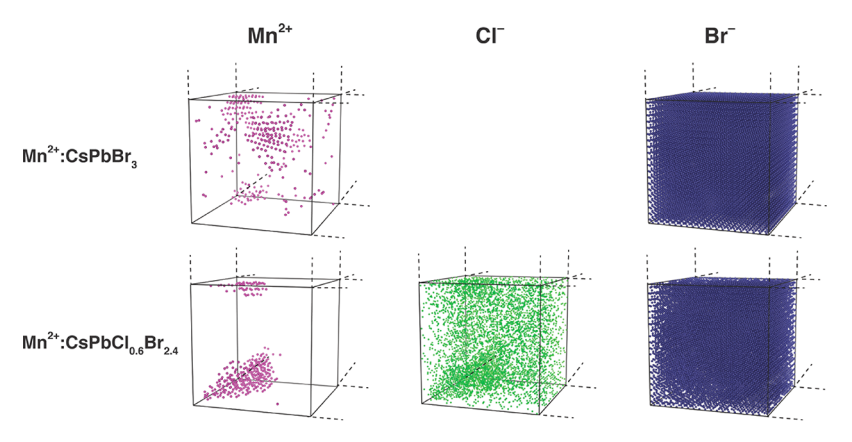
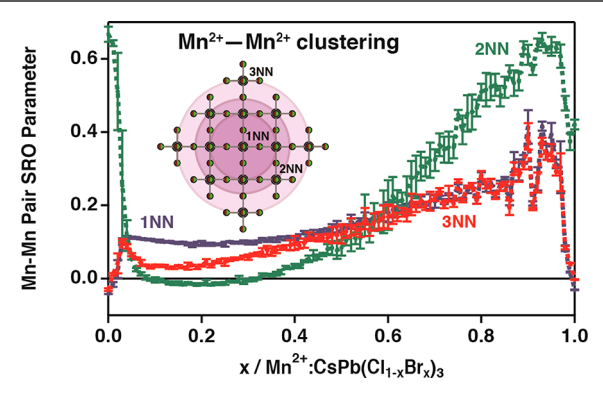


Figure 6. Distribution of atoms within a 4%  $Mn^{2+}$ :  $CsPb(Cl_{1-x}Br_x)_3$  supercell for x = 1.0 (top) and 0.8 (bottom). The distributions of  $Mn^{2+}$ ,  $Cl^-$ , and  $Br^-$  ions are shown.



**Figure 7.** Short-range order (SRO) parameters for 1NN, 2NN, and 3NN  $\rm Mn^{2+}{-}\rm Mn^{2+}$  pairs in 4%  $\rm Mn^{2+}{:}\rm CsPb(Cl_{1-x}\rm Br_x)_3$  plotted vs the halide composition parameter x, as predicted by cluster-expansion canonical Monte Carlo methods. Spinodal decomposition is observed at both x=0 and x=1, and  $\rm Mn^{2+}{-}\rm Mn^{2+}$  1NN clustering is observed when x>0. The SRO oscillations near x=1.0 are due to fluctuations between competing low-energy cluster configurations. The inset shows the 1NN, 2NN, and 3NN sites around a central cation, with chloride/bromide ions depicted in green/brown and lead/manganese ions depicted in gray.

parameter x. Interestingly, the pure and dilute chloride compositions both show segregation of ordered Mn<sup>2+</sup>-rich domains characterized by Mn<sup>2+</sup>-Mn<sup>2+</sup> pairs occupying 2NN sites. The decomposition of an initially random mixture into coexisting Mn<sup>2+</sup>-enriched and -depleted domains, i.e., spinodal decomposition, suggests a tendency for each Mn<sup>2+</sup> to maximize its number of Pb2+ nearest neighbors in the absence of significant halide mixing. The stability of the Mn<sup>2+</sup>-enriched phase is consistent with a simple model of Coulomb energy gain. In this picture, there is a transfer of partial charge,  $\delta$ , between Mn<sup>2+</sup> and Pb<sup>2+</sup> nearest neighbors due to their different electronegativities and the high ionicity of the lattice. This transfer leads to nominal oxidation states of  $Pb^{(2-\delta)+}$  and  $Mn^{(2+\delta)+}$ , and it lowers the Coulomb energy by an amount proportional to  $-\delta^2/2r$ , where 2r is the distance between the Pb<sup>2+</sup> and Mn<sup>2+</sup> ions. The configuration that maximizes the number of 1NN Mn<sup>2+</sup>-Pb<sup>2+</sup> pairs maximizes this Coulomb energy gain. The optimal configuration thus corresponds to Mn<sup>2+</sup>-Mn<sup>2+</sup> pairs ordered on 2NN sites. Using DFT and Bader charge analysis,<sup>72</sup> the average charge transferred between 1NN  $Mn^{2+}$  and  $Pb^{2+}$  is  $\delta = 0.21$  and 0.19 in the cases of Cs<sub>2</sub>PbMnCl<sub>6</sub> and Cs<sub>2</sub>PbMnBr<sub>6</sub>, respectively. This

2NN ordering may also reduce the lattice strain associated with substituting  $Pb^{2+}$  with the smaller  $Mn^{2+}$ , leading to further stabilization relative to the random alloy. Because superexchange is only a short-range interaction, superexchange coupling between 2NN  $Mn^{2+}$  ions is negligible and 2NN ordering therefore cannot explain the experimental clustering concluded from the loss of EPR intensity in Figure 3. To explain this observation, 1NN  $Mn^{2+}$ – $Mn^{2+}$  clustering is required.

For x = 0, the MC simulations predict no 1NN  $Mn^{2+}-Mn^{2+}$ clustering. Figure 7 shows a rapid increase in 1NN clustering with  $Br^-$  addition in the dilute-bromide limit (small x), followed by nonlinear and generally increasing 1NN clustering with increasing Br concentration. Indeed, clustering at all Mn<sup>2+</sup>-Mn<sup>2+</sup> separations (1NN, 2NN, 3NN) generally increases with increasing x, consistent with  $Mn^{2+}$  segregation into enriched crystalline domains as Br is added to the lattice. Moreover, the modeling further predicts that Cl- will also cluster with increasing x and specifically that the Mn<sup>2+</sup> and Cl<sup>-</sup> ions are themselves correlated. For example, Figure 8 plots 1NN and 2NN Mn-Cl and Mn-Br SRO parameters as a function of x. These results show that  $Mn^{2+}$ – $Cl^-$  correlations increase and  $\mathrm{Mn^{2+}}\mathrm{-Br^{-}}$  correlations decrease with increasing x(see Figure S12 for Cl<sup>-</sup>-Cl<sup>-</sup> and Br<sup>-</sup>-Br<sup>-</sup> SRO plots). Although the results generally show anticorrelation for Mn<sup>2+</sup>-Br pairs, there is in fact an initial positive correlation at low bromide concentrations that may result from a slight energy stabilization associated with relieving lattice strain by having a smaller Mn<sup>2+</sup> dopant next to a larger bromide ion. Overall, these results support the two key conclusions drawn from the experimental results, namely, that 1NN Mn<sup>2+</sup> clustering occurs with increasing x in Mn<sup>2+</sup>:CsPb(Cl<sub>1-x</sub>Br<sub>x</sub>)<sub>3</sub> NCs (Figure 3C) and that Mn<sup>2+</sup> remains coordinated by Cl<sup>-</sup> despite the addition of Br<sup>-</sup> to the lattice (Figure 3D).

## DISCUSSION

The experimental and computational results presented above provide strong evidence of  $\mathrm{Mn^{2+}}$  clustering in  $\mathrm{Mn^{2+}}$ :CsPb- $(\mathrm{Cl_{1-x}Br_x})_3$  NCs induced by  $\mathrm{Cl^-} \to \mathrm{Br^-}$  anion exchange.  $\mathrm{Mn^{2+}}$  is highly mobile in  $\mathrm{Mn^{2+}}$ :CsPb( $\mathrm{Cl_{1-x}Br_x})_3$  NCs, suggesting that clustering is driven thermodynamically not kinetically. A simple qualitative explanation for this observation can be proposed within the framework of hard–soft acid–base (HSAB) theory. As a hard Lewis acid,  $\mathrm{Mn^{2+}}$  has a stronger preference for hard  $\mathrm{Cl^-}$  (Lewis base) ligands relative to softer

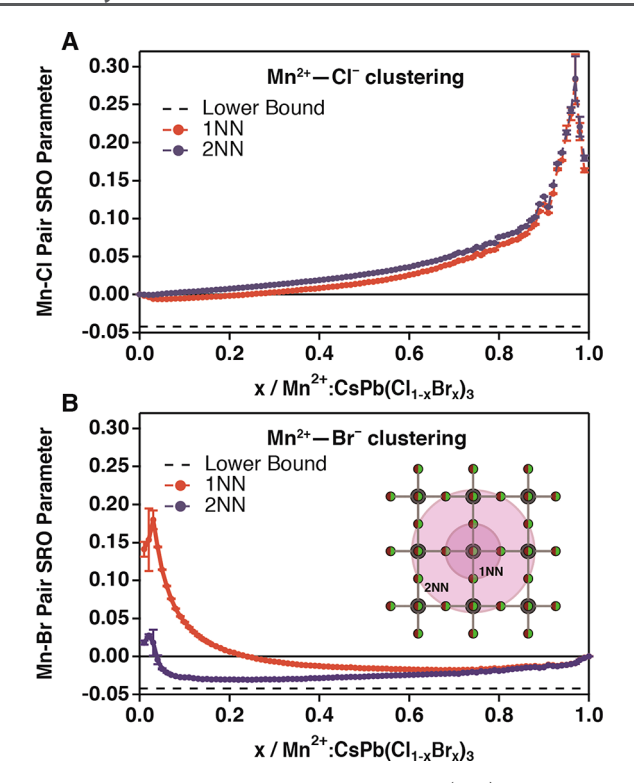


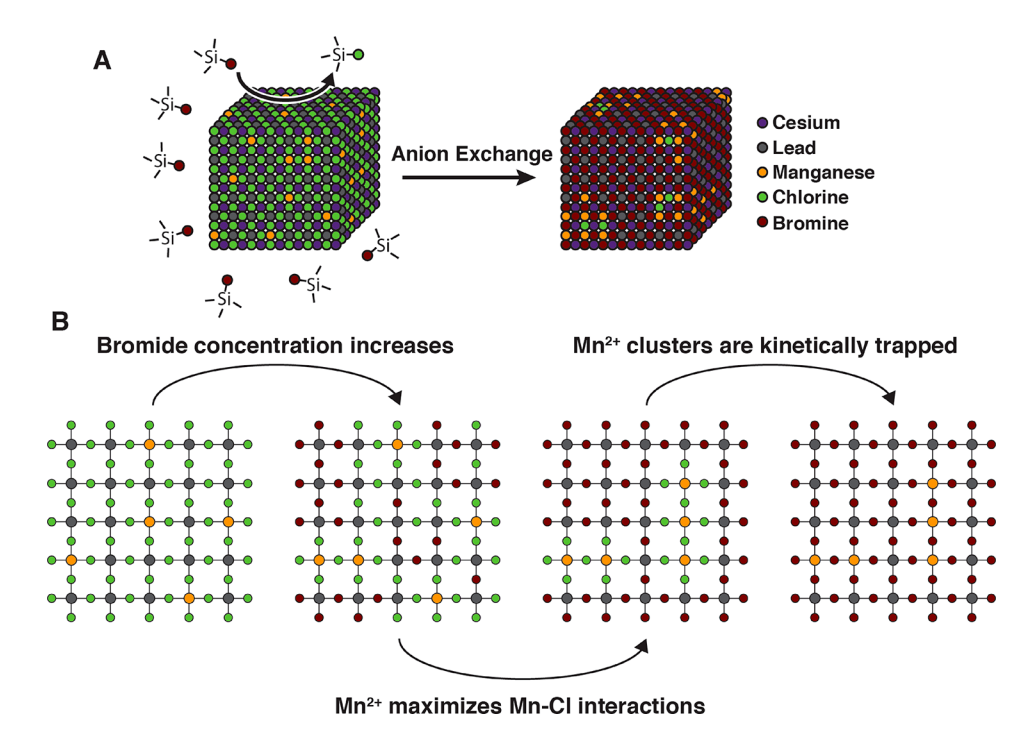
**Figure 8.** Short-range order (SRO) parameters  $\eta_i^{(XlMn)}$  for (A) Mn<sup>2+</sup>–Cl<sup>-</sup> and (B) Mn<sup>2+</sup>–Br<sup>-</sup> pairs in 4% Mn<sup>2+</sup>:CsPb(Cl<sub>1-x</sub>Br<sub>x</sub>)<sub>3</sub>, plotted vs the halide composition parameter x, as predicted by canonical Monte Carlo simulations. Mn<sup>2+</sup>–Cl<sup>-</sup> clustering becomes more pronounced as more Br<sup>-</sup> is incorporated. The inset shows the 1NN and 2NN sites around a central cation, with chloride/bromide ions depicted in green/brown and lead/manganese ions depicted in gray.

 $Br^-$  ligands. The specific preference of  $Mn^{2+}$  for  $CsPbCl_3$  compared to  $CsPbBr_3$  is evident from the facile incorporation of  $Mn^{2+}$  into the former  $^{16,24,25}$  and the inability to easily

introduce Mn<sup>2+</sup> into the latter either by direct synthesis or by cation exchange. <sup>6,23</sup> We propose that this preference is a primary driving force behind the Mn<sup>2+</sup> clustering we have observed experimentally in Figure 3C. Such considerations suggest that, as the lattice Cl<sup>-</sup> concentration decreases, Mn<sup>2+</sup> dopants migrate in order to retain their preferred Mn–Cl bonding, eventually requiring two or more Mn<sup>2+</sup> ions to bind to the same Cl<sup>-</sup> anion, in turn increasing the prevalence of 1NN Mn<sup>2+</sup>–Mn<sup>2+</sup> pairs and their associated antiferromagnetic superexchange coupling. This process is summarized in Scheme 1.

The MC simulations support this interpretation, showing positive and increasing Mn<sup>2+</sup>-Mn<sup>2+</sup> 1NN and Mn<sup>2+</sup>-Cl<sup>-</sup> 1NN correlations upon introduction of Br into a Mn<sup>2+</sup>:CsPbCl<sub>3</sub> lattice. This situation is an example of spinodal decomposition, in which the free energy of an unstable solid solution is reduced by separating into coexisting phases. This segregation is driven in part by the difference between Mn-Cl and Mn-Br bond enthalpies. Beyond supporting the experimental conclusion of Br-induced Mn2+ clustering in Mn2+:CsPb- $(Cl_{1-x}Br_x)_3$  NCs, the MC simulations reveal additional insights not detected experimentally. In particular, the modeling predicts that 2NN Mn<sup>2+</sup>-Mn<sup>2+</sup> ordering is already thermodynamically favored even at the composition end points of Mn<sup>2+</sup>:CsPbCl<sub>3</sub> and Mn<sup>2+</sup>:CsPbBr<sub>3</sub>. The clustering in these compositions has a strong preference for ordering at the 2NN site, driven by Coulomb interactions and potentially strain minimization. This 2NN ordering cannot explain the Brinduced loss of EPR intensity, however; antiferromagnetic superexchange coupling requires 1NN Mn<sup>2+</sup>-Mn<sup>2+</sup> interactions. Although 1NN Mn<sup>2+</sup>-Mn<sup>2+</sup> interactions are not observed or predicted in the CsPbCl3 limit under the conditions examined here, these conditions differ substantially from those that caused formation of spinodal CsMnCl<sub>3</sub> phases in CsPbCl<sub>3</sub> nanoplatelets, which involved prolonged 200 °C solvothermal diffusion doping in the presence of high solvated

Scheme 1. Proposed Manganese Clustering during Cl<sup>-</sup> → Br<sup>-</sup> Anion Exchange in Mn<sup>2+</sup>:CsPbCl<sub>3</sub> NCs



Mn<sup>2+</sup> concentrations;<sup>32</sup> the present study provides further evidence of condition-dependent nonrandom Mn<sup>2+</sup> distributions within doped perovskite NCs.

The conclusions drawn here are based on thermodynamics and should be largely generalizable to bulk and nanocrystalline  $Mn^{2+}$ :CsPb(Cl<sub>1-x</sub>Br<sub>x</sub>)<sub>3</sub> prepared by different routes or to  $Mn^{2+}$ :CsPb(Cl<sub>1-x</sub>Br<sub>x</sub>)<sub>3</sub> NC anion-exchange reactions involving different anion precursors. Still, a kinetic factor is also apparent in the observation that the 1NN Mn<sup>2+</sup>-Mn<sup>2+</sup> clustering induced by partial  $Cl^- \rightarrow Br^-$  anion exchange is not lost again upon complete conversion to CsPbBr3, where computations suggest the 2NN spinodal ordering would be more stable. The stability of isolated Mn<sup>2+</sup> in CsPbBr<sub>3</sub> is supported by the observation of Mn2+ EPR hyperfine splittings in bulk Mn<sup>2+</sup>:CsPbBr<sub>3</sub> prepared by direct synthesis (see Figure S6). This apparent reduction in Mn<sup>2+</sup> mobility may be associated with the requirement of cation vacancies for cation migration in these lattices, a requirement that is more readily met during anion exchange than under static conditions.

The large structural reorganization and  $Mn^{2+}$  clustering in  $Mn^{2+}$ :CsPb( $Cl_{1-x}Br_x$ )<sub>3</sub> NCs with anion exchange may impact the physical properties of these materials broadly. For example, the loss of  $Mn^{2+}$  EPR described here suggests that anion exchange converts paramagnetic  $Mn^{2+}$ :CsPbCl<sub>3</sub> NCs into antiferromagnetic  $Mn^{2+}$ :CsPb( $Cl_{1-x}Br_x$ )<sub>3</sub> NCs, which should fundamentally alter the magneto-optical or magneto-transport responses of these materials. Additionally, this  $Mn^{2+}$  clustering complicates interpretation of the characteristic x dependence of  $Mn^{2+}$  and excitonic PL intensities in  $Mn^{2+}$ :CsPb( $Cl_{1-x}Br_x$ )<sub>3</sub> NCs noted in several publications,  $^{6,26-28}$  because  $Mn^{2+}$  clustering alters  $Mn^{2+}$  radiative decay rates,  $Mn^{2+}$  nonradiative decay rates, and very likely also exciton-to- $Mn^{2+}$  energy-transfer rates.

## CONCLUSION

In summary, we have studied anion exchange in Mn<sup>2+</sup>-doped  $CsPb(Cl_{1-x}Br_x)_3$  NCs by PL and EPR spectroscopies. During the course of Cl<sup>-</sup> → Br<sup>-</sup> anion exchange, we observed the disappearance of the Mn2+ EPR signal despite retention of strong Mn<sup>2+</sup>-based PL. These results are interpreted as reflecting clustering of Mn2+ dopants during anion exchange to form antiferromagnetically coupled dimers or highernuclearity clusters. The thermodynamic driving force for this clustering comes from the stronger Mn-Cl bonding compared to Mn-Br bonding, in keeping with HSAB principles. The EPR hyperfine splittings measured during anion exchange confirm retention of Mn-Cl bonding even when the majority of lattice anions are bromides. DFT-based Monte Carlo modeling supports these conclusions, predicting strongly correlated Mn<sup>2+</sup> and Cl<sup>-</sup> segregation as bromide is added to the lattice. Monte Carlo modeling further suggests that spinodal decomposition to form ordered Mn2+-enriched domains is thermodynamically favorable even at the CsPbCl<sub>3</sub> and CsPbBr3 end points of the lattice anion exchange reaction. Mn2+ ions are predicted to occupy second-nearest-neighbor positions relative to one another in these spinodal domains.

Overall, these experimental and computational results provide strong evidence that cationic dopants in metal-halide perovskites are generally distributed nonrandomly, with dynamic spatial distributions that depend on the lattice's anion composition. Although not explicitly tested here, this conclusion likely extends to other cationic impurities beyond Mn<sup>2+</sup>, and it likely applies to both bulk and nanostructured

perovskites. The high mobility of both cations and anions in perovskite NCs contrasts the behavior established in chalcogenide semiconductor NCs such as CdSe,  $Cu_{2-x}S$ , or PbS, where cation exchange typically occurs without substantial perturbation of the anion sublattice. The findings here of dynamic anion-dependent cation distributions within doped perovskite NCs impact the understanding of the stability and electronic or photophysical properties of such doped perovskites, which in turn has ramifications for how these and related metal-halide semiconductor materials may be used in future optoelectronic technologies.

#### ASSOCIATED CONTENT

# S Supporting Information

The Supporting Information is available free of charge on the ACS Publications website at DOI: 10.1021/acs.chemmater.9b02646.

Elemental analysis, normalized RT PL spectra during anion exchange, additional room-temperature and low-temperature EPR spectra during anion-exchange reactions, data from Mn(oleate)<sub>2</sub> addition, EPR spectra and XRD data for bulk Mn<sup>2+</sup>:CsPbBr<sub>3</sub> powder, absorbance and variable-temperature PL spectra for doped nanocrystals, additional computational results and discussion, and <sup>133</sup>Cs NMR results and discussion (PDF)

#### AUTHOR INFORMATION

# **Corresponding Author**

\*E-mail: gamelin@chem.washington.edu.

#### ORCID (

Sidney E. Creutz: 0000-0003-4440-5336 Daniel R. Gamelin: 0000-0003-2888-9916

### **Present Address**

<sup>L</sup>S.E.C.: Department of Chemistry, Mississippi State University, Box 9573, Mississippi State, Mississippi 39762.

#### Notes

The authors declare no competing financial interest.

#### ACKNOWLEDGMENTS

Dr. Adrienne Roehrich is gratefully acknowledged for assistance with the ssNMR measurements. This research was supported by the National Science Foundation (NSF) through the UW Molecular Engineering Materials Center, a Materials Research Science and Engineering Center (DMR-1719797 to D.R.G. and S.T.D.), and through DMR-1807394 (to D.R.G.). Additional support from an appointment to the Intelligence Community Postdoctoral Research Fellowship Program at UW (SEC), administered by Oak Ridge Institute for Science and Education through an interagency agreement between the U.S. Department of Energy and the Office of the Director of National Intelligence, is gratefully acknowledged. Part of this work was conducted at the Molecular Analysis Facility, a National Nanotechnology Coordinated Infrastructure site at the University of Washington that is supported in part by the National Science Foundation (grant ECC-1542101), the University of Washington, the Molecular Engineering & Sciences Institute, the Clean Energy Institute, and the National Institutes of Health. This work was facilitated though the use of advanced computational, storage, and networking infrastructure provided by the Hyak supercomputer system and funded by the STF at the University of Washington.

## **■** REFERENCES

- (1) Protesescu, L.; Yakunin, S.; Bodnarchuk, M. I.; Krieg, F.; Caputo, R.; Hendon, C. H.; Yang, R. X.; Walsh, A.; Kovalenko, M. V. Nanocrystals of Cesium Lead Halide Perovskites (CsPbX<sub>3</sub>, X = Cl, Br, and I): Novel Optoelectronic Materials Showing Bright Emission with Wide Color Gamut. *Nano Lett.* **2015**, *15*, 3692–6.
- (2) Akkerman, Q. A.; Rainò, G.; Kovalenko, M. V.; Manna, L. Genesis, challenges and opportunities for colloidal lead halide perovskite nanocrystals. *Nat. Mater.* **2018**, *17*, 394–405.
- (3) Kang, J.; Wang, L.-W. High Defect Tolerance in Lead Halide Perovskite CsPbBr3. *J. Phys. Chem. Lett.* **2017**, *8*, 489–493.
- (4) Li, X.; Wu, Y.; Zhang, S.; Cai, B.; Gu, Y.; Song, J.; Zeng, H. CsPbX<sub>3</sub> Quantum Dots for Lighting and Displays: Room-Temperature Synthesis, Photoluminescence Superiorities, Underlying Origins and White Light-Emitting Diodes. *Adv. Funct. Mater.* **2016**, 26, 2435–2445.
- (5) Zhang, X.; Lin, H.; Huang, H.; Reckmeier, C.; Zhang, Y.; Choy, W. C. H.; Rogach, A. L. Enhancing the Brightness of Cesium Lead Halide Perovskite Nanocrystal Based Green Light-Emitting Devices through the Interface Engineering with Perfluorinated Ionomer. *Nano Lett.* 2016, 16, 1415.
- (6) Liu, W.; Lin, Q.; Li, H.; Wu, K.; Robel, I.; Pietryga, J. M.; Klimov, V. I. Mn<sup>2+</sup>-Doped Lead Halide Perovskite Nanocrystals with Dual-Color Emission Controlled by Halide Content. *J. Am. Chem. Soc.* **2016**, *138*, 14954–14961.
- (7) Swarnkar, A.; Marshall, A. R.; Sanehira, E. M.; Chernomordik, B. D.; Moore, D. T.; Christians, J. A.; Chakrabarti, T.; Luther, J. M. Quantum dot-induced phase stabilization of  $\alpha$ -CsPbI<sub>3</sub> perovskite for high-efficiency photovoltaics. *Science* **2016**, *354*, 92–95.
- (8) Akkerman, Q. A.; Gandini, M.; Di Stasio, F.; Rastogi, P.; Palazon, F.; Bertoni, G.; Ball, J. M.; Prato, M.; Petrozza, A.; Manna, L. Strongly emissive perovskite nanocrystal inks for high-voltage solar cells. *Nat. Energy* **2017**, *2*, 16194.
- (9) Zhang, J.; Wang, Q.; Zhang, X.; Jiang, J.; Gao, Z.; Jin, Z.; Liu, S. High-performance transparent ultraviolet photodetectors based on inorganic perovskite CsPbCl<sub>3</sub> nanocrystals. *RSC Adv.* **2017**, 7, 36722–36727.
- (10) Miao, J.; Zhang, F. Recent progress on highly sensitive perovskite photodetectors. *J. Mater. Chem. C* **2019**, *7*, 1741–1791.
- (11) Nedelcu, G.; Protesescu, L.; Yakunin, S.; Bodnarchuk, M. I.; Grotevent, M. J.; Kovalenko, M. V. Fast Anion-Exchange in Highly Luminescent Nanocrystals of Cesium Lead Halide Perovskites (CsPbX<sub>3</sub>, X = Cl, Br, I). *Nano Lett.* **2015**, *15*, 5635–5640.
- (12) Akkerman, Q. A.; D'Innocenzo, V.; Accornero, S.; Scarpellini, A.; Petrozza, A.; Prato, M.; Manna, L. Tuning the Optical Properties of Cesium Lead Halide Perovskite Nanocrystals by Anion Exchange Reactions. J. Am. Chem. Soc. 2015, 137, 10276–10281.
- (13) Parobek, D.; Roman, B. J.; Dong, Y.; Jin, H.; Lee, E.; Sheldon, M.; Son, D. H. Exciton-to-Dopant Energy Transfer in Mn-Doped Cesium Lead Halide Perovskite Nanocrystals. *Nano Lett.* **2016**, *16*, 7376–7380.
- (14) Guria, A. K.; Dutta, S. K.; Adhikari, S. D.; Pradhan, N. Doping Mn<sup>2+</sup> in Lead Halide Perovskite Nanocrystals: Successes and Challenges. *ACS Energy Lett.* **2017**, *2*, 1014–1021.
- (15) Xu, K.; Lin, C. C.; Xie, X.; Meijerink, A. Efficient and Stable Luminescence from Mn<sup>2+</sup> in Core and Core-Isocrystalline Shell CsPbCl<sub>3</sub> Perovskite Nanocrystals. *Chem. Mater.* **2017**, *29*, 4265–4272.
- (16) Mir, W. J.; Mahor, Y.; Lohar, A.; Jagadeeswararao, M.; Das, S.; Mahamuni, S.; Nag, A. Postsynthesis Doping of Mn and Yb into CsPbX<sub>3</sub> (X = Cl, Br, or I) Perovskite Nanocrystals for Downconversion Emission. *Chem. Mater.* **2018**, *30*, 8170–8178.
- (17) Pan, G.; Bai, X.; Yang, D.; Chen, X.; Jing, P.; Qu, S.; Zhang, L.; Zhou, D.; Zhu, J.; Xu, W.; Dong, B.; Song, H. Doping Lanthanide into Perovskite Nanocrystals: Highly Improved and Expanded Optical Properties. *Nano Lett.* **2017**, *17*, 8005–8011.
- (18) Milstein, T. J.; Kroupa, D. M.; Gamelin, D. R. Picosecond Quantum Cutting Generates Photoluminescence Quantum Yields

Over 100% in Ytterbium-Doped CsPbCl<sub>3</sub> Nanocrystals. *Nano Lett.* **2018**, *18*, 3792–3799.

- (19) Li, F.; Xia, Z.; Pan, C.; Gong, Y.; Gu, L.; Liu, Q.; Zhang, J. Z. High Br<sup>-</sup> Content CsPb(Cl<sub>y</sub>Br<sub>1-y</sub>)<sub>3</sub> Perovskite Nanocrystals with Strong Mn<sup>2+</sup> Emission through Diverse Cation/Anion Exchange Engineering. ACS Appl. Mater. Interfaces **2018**, 10, 11739–11746.
- (20) Chen, D.; Fang, G.; Chen, X. Silica-Coated Mn-Doped CsPb(Cl/Br)<sub>3</sub> Inorganic Perovskite Quantum Dots: Exciton-to-Mn Energy Transfer and Blue-Excitable Solid-State Lighting. *ACS Appl. Mater. Interfaces* **2017**, *9*, 40477–40487.
- (21) Meinardi, F.; Akkerman, Q. A.; Bruni, F.; Park, S.; Mauri, M.; Dang, Z.; Manna, L.; Brovelli, S. Doped Halide Perovskite Nanocrystals for Reabsorption-Free Luminescent Solar Concentrators. ACS Energy Lett. 2017, 2, 2368–2377.
- (22) Wang, Q.; Zhang, X.; Jin, Z.; Zhang, J.; Gao, Z.; Li, Y.; Liu, S. F. Energy-Down-Shift CsPbCl<sub>3</sub>:Mn Quantum Dots for Boosting the Efficiency and Stability of Perovskite Solar Cells. *ACS Energy Lett.* **2017**, *2*, 1479–1486.
- (23) Parobek, D.; Dong, Y.; Qiao, T.; Son, D. H. Direct Hot-Injection Synthesis of Mn-Doped CsPbBr<sub>3</sub> Nanocrystals. *Chem. Mater.* **2018**, *30*, 2939.
- (24) Gao, D.; Qiao, B.; Xu, Z.; Song, D.; Song, P.; Liang, Z.; Shen, Z.; Cao, J.; Zhang, J.; Zhao, S. Postsynthetic, Reversible Cation Exchange between Pb<sup>2+</sup> and Mn<sup>2+</sup> in Cesium Lead Chloride Perovskite Nanocrystals. *J. Phys. Chem. C* **2017**, *121*, 20387–20395.
- (25) Xu, W.; Li, F.; Lin, F.; Chen, Y.; Cai, Z.; Wang, Y.; Chen, X. Synthesis of CsPbCl<sub>3</sub>-Mn Nanocrystals via Cation Exchange. *Adv. Opt. Mater.* **2017**, *5*, 1700520.
- (26) Xu, K.; Meijerink, A. Tuning Exciton-Mn<sup>2+</sup> Energy Transfer in Mixed Halide Perovskite Nanocrystals. *Chem. Mater.* **2018**, *30*, 5346–5352.
- (27) Mir, W. J.; Jagadeeswararao, M.; Das, S.; Nag, A. Colloidal Mn-Doped Cesium Lead Halide Perovskite Nanoplatelets. *ACS Energy Lett.* **2017**, *2*, 537–543.
- (28) Fei, L.; Yuan, X.; Hua, J.; Ikezawa, M.; Zeng, R.; Li, H.; Masumoto, Y.; Zhao, J. Enhanced luminescence and energy transfer in Mn<sup>2+</sup> doped CsPbCl<sub>3-x</sub>Br<sub>x</sub> perovskite nanocrystals. *Nanoscale* **2018**, *10*, 19435–19442.
- (29) Li, G.; Ho, J. Y.-L.; Wong, M.; Kwok, H. S. Reversible Anion Exchange Reaction in Solid Halide Perovskites and Its Implication in Photovoltaics. *J. Phys. Chem. C* **2015**, *119*, 26883–26888.
- (30) van der Stam, W.; Geuchies, J. J.; Altantzis, T.; van den Bos, K. H. W.; Meeldijk, J. D.; Van Aert, S.; Bals, S.; Vanmaekelbergh, D.; de Mello Donega, C. Highly Emissive Divalent Ion Doped Colloidal CsPb<sub>1-x</sub>M<sub>x</sub>Br<sub>3</sub> Perovskite Nanocrystals through Cation Exchange. *J. Am. Chem. Soc.* **2017**, *139*, 4087–4097.
- (31) Li, M.; Zhang, X.; Matras-Postolek, K.; Chen, H.-S.; Yang, P. An anion-driven Sn<sup>2+</sup> exchange reaction in CsPbBr<sub>3</sub> nanocrystals towards tunable and high photoluminescence. *J. Mater. Chem. C* **2018**, *6*, 5506–5513.
- (32) Li, Z.-J.; Hofman, E.; Davis, A. H.; Khammang, A.; Wright, J. T.; Dzikovski, B.; Meulenberg, R. W.; Zheng, W. Complete Dopant Substitution by Spinodal Decomposition in Mn-Doped Two-Dimensional CsPbCl<sub>3</sub> Nanoplatelets. *Chem. Mater.* **2018**, *30*, 6400–6409.
- (33) Kubicki, D. J.; Prochowicz, D.; Pinon, A.; Stevanato, G.; Hofstetter, A.; Zakeeruddin, S. M.; Grätzel, M.; Emsley, L. Doping and phase segregation in Mn<sup>2+</sup>- and Co<sup>2+</sup>-doped lead halide perovskites from <sup>133</sup>Cs and <sup>1</sup>H NMR relaxation enhancement. *J. Mater. Chem. A* **2019**, *7*, 2326–2333.
- (34) Puglisi, A.; Mondini, S.; Cenedese, S.; Ferretti, A. M.; Santo, N.; Ponti, A. Monodisperse Octahedral  $\alpha$ -MnS and MnO Nanoparticles by the Decomposition of Manganese Oleate in the Presence of Sulfur. *Chem. Mater.* **2010**, 22, 2804–2813.
- (35) Wong, A.; Sham, S.; Wang, S.; Wu, G. A solid-state <sup>133</sup>Cs nuclear magnetic resonance and X-ray crystallographic study of cesium complexes with macrocyclic ligands. *Can. J. Chem.* **2000**, *78*, 975–985.

(36) Hart, G. L. W.; Forcade, R. W. Algorithm for generating derivative structures. *Phys. Rev. B: Condens. Matter Mater. Phys.* **2008**, 77, 224115.

- (37) Sanchez, J. M.; Ducastelle, F.; Gratias, D. Generalized cluster description of multicomponent systems. *Phys. A* **1984**, *128*, 334–350.
- (38) van de Walle, A. Multicomponent multisublattice alloys, nonconfigurational entropy and other additions to the Alloy Theoretic Automated Toolkit. *CALPHAD: Comput. Coupling Phase Diagrams Thermochem.* **2009**, 33, 266–278.
- (39) Nelson, L. J.; Hart, G. L. W.; Zhou, F.; Ozolinš, V. Compressive sensing as a paradigm for building physics models. *Phys. Rev. B: Condens. Matter Mater. Phys.* **2013**, 87, 035125.
- (40) CASMcode: v0.2.1; 2017; DOI: 10.5281/zenodo.546148.
- (41) Puchala, B.; Van der Ven, A. Thermodynamics of the Zr-O system from first-principles calculations. *Phys. Rev. B: Condens. Matter Mater. Phys.* **2013**, *88*, 094108.
- (42) Van der Ven, A.; Thomas, J. C.; Xu, Q.; Bhattacharya, J. Linking the electronic structure of solids to their thermodynamic and kinetic properties. *Math. Comput. Simul.* **2010**, *80*, 1393–1410.
- (43) van de Walle, A.; Ceder, G. Automating first-principles phase diagram calculations. *J. Phase Equilib.* **2002**, *23*, 348.
- (44) van de Walle, A.; Asta, M. Self-driven lattice-model Monte Carlo simulations of alloy thermodynamic properties and phase diagrams. *Modell. Simul. Mater. Sci. Eng.* **2002**, *10*, 521.
- (45) Pedregosa, F.; Varoquaux, G.; Gramfort, A.; Michel, V.; Thirion, B.; Grisel, O.; Blondel, M.; Prettenhofer, P.; Weiss, R.; Dubourg, V.; Vanderplas, J.; Passos, A.; Cournapeau, D.; Brucher, M.; Perrot, M.; Duchesnay, É. Scikit-learn: Machine Learning in Python. *J. Mach. Learn. Res.* **2011**, *12*, 2825–2830.
- (46) Kresse, G.; Hafner, J. Norm-conserving and ultrasoft pseudopotentials for first-row and transition elements. *J. Phys.: Condens. Matter* **1994**, *6*, 8245.
- (47) Kresse, G.; Joubert, D. From ultrasoft pseudopotentials to the projector augmented-wave method. *Phys. Rev. B: Condens. Matter Mater. Phys.* **1999**, *59*, 1758–1775.
- (48) Kresse, G.; Furthmüller, J. Efficient iterative schemes for ab initio total-energy calculations using a plane-wave basis set. *Phys. Rev. B: Condens. Matter Mater. Phys.* **1996**, *54*, 11169–11186.
- (49) Kresse, G.; Furthmüller, J. Efficiency of ab-initio total energy calculations for metals and semiconductors using a plane-wave basis set. *Comput. Mater. Sci.* **1996**, *6*, 15–50.
- (50) Blöchl, P. E. Projector augmented-wave method. *Phys. Rev. B: Condens. Matter Mater. Phys.* **1994**, *50*, 17953–17979.
- (51) Perdew, J. P.; Burke, K.; Ernzerhof, M. Generalized Gradient Approximation Made Simple. *Phys. Rev. Lett.* **1996**, 77, 3865–3868.
- (52) Monkhorst, H. J.; Pack, J. D. Special points for Brillouin-zone integrations. *Phys. Rev. B* **1976**, *13*, 5188–5192.
- (53) Zou, S.; Liu, Y.; Li, J.; Liu, C.; Feng, R.; Jiang, F.; Li, Y.; Song, J.; Zeng, H.; Hong, M.; Chen, X. Stabilizing Cesium Lead Halide Perovskite Lattice through Mn (II)-Substitution for Air-Stable Light-Emitting Diodes. *J. Am. Chem. Soc.* **2017**, *139*, 11443–11450.
- (54) Yuan, X.; Ji, S.; De Siena, M. C.; Fei, L.; Zhao, Z.; Wang, Y.; Li, H.; Zhao, J.; Gamelin, D. R. Photoluminescence Temperature Dependence, Dynamics, and Quantum Efficiencies in Mn<sup>2+</sup>-Doped CsPbCl<sub>3</sub> Perovskite Nanocrystals with Varied Dopant Concentration. *Chem. Mater.* **2017**, 29, 8003–8011.
- (55) Creutz, S. E.; Crites, E. N.; De Siena, M. C.; Gamelin, D. R. Colloidal Nanocrystals of Lead-Free Double-Perovskite (Elpasolite) Semiconductors: Synthesis and Anion Exchange To Access New Materials. *Nano Lett.* **2018**, *18*, 1118–1123.
- (56) Creutz, S. E.; Crites, E. N.; De Siena, M. C.; Gamelin, D. R. Anion Exchange in Cesium Lead Halide Perovskite Nanocrystals and Thin Films Using Trimethylsilyl Halide Reagents. *Chem. Mater.* **2018**, 30, 4887–4891.
- (57) Li, F.; Xia, Z.; Gong, Y.; Gu, L.; Liu, Q. Optical properties of Mn<sup>2+</sup> doped cesium lead halide perovskite nanocrystals via a cationanion co-substitution exchange reaction. *J. Mater. Chem. C* **2017**, *S*, 9281–9287.

- (58) Nenon, D. P.; Pressler, K.; Kang, J.; Koscher, B. A.; Olshansky, J. H.; Osowiecki, W. T.; Koc, M. A.; Wang, L.-W.; Alivisatos, A. P. Design Principles for Trap-Free CsPbX<sub>3</sub> Nanocrystals: Enumerating and Eliminating Surface Halide Vacancies with Softer Lewis Bases. J. Am. Chem. Soc. 2018, 140, 17760–17772.
- (59) Beaulac, R.; Archer, P. I.; van Rijssel, J.; Meijerink, A.; Gamelin, D. R. Exciton Storage by Mn2+ in Colloidal Mn2+-Doped CdSe Quantum Dots. *Nano Lett.* **2008**, *8*, 2949–2953.
- (60) Vlaskin, V. A.; Janßen, N.; van Rijssel, J.; Beaulac, R.; Gamelin, D. R. Tunable Dual Emission in Doped Semiconductor Nanocrystals. *Nano Lett.* **2010**, *10*, 3670–3674.
- (61) Matumura, O. Electron Spin Resonance of Mn-activated Phosphors. J. Phys. Soc. Jpn. 1959, 14, 108.
- (62) Šimánek, E.; Müller, K. A. Covalency and hyperfine structure constant A of iron group impurities in crystals. *J. Phys. Chem. Solids* 1970, 31, 1027–1040.
- (63) Gupta, R. P.; Seehra, M. S.; Vehse, W. E. Shift of Néel Temperature and EPR Linewidth of KMnF<sub>3</sub> with Mg Doping. *Phys. Rev. B* **1972**, *5*, 92–95.
- (64) Krebs, J. J. EPR Determination of the Nearest-Neighbor Exchange Constant for Mn<sup>2+</sup> Pairs in KZnF<sub>3</sub>. *J. Appl. Phys.* **1969**, *40*, 1137–1139.
- (65) King, R. B., Crabtree, R. H., Lukehart, C. M., Atwood, D. A., Scott, R. A., Eds. Bond Energies. In *Encyclopedia of Inorganic Chemistry*; Wiley: 2006; DOI: 10.1002/0470862106.id098.
- (66) De Lucas, M. C. M.; Rodríguez, F.; Prieto, C.; Verdaguer, M.; Moreno, M.; Güdel, H. U. Optical properties and local structure of MnCl<sub>6</sub><sup>4-</sup> in ABCl<sub>3</sub>:Mn<sup>2+</sup>. *Radiat. Eff. Defects Solids* **1995**, *135*, 95–100.
- (67) McPherson, G. L.; Waguespack, Y. Y.; Vanoy, T. C.; Rodriguez, W. J. Exciton migration in a "pseudo"-one-dimensional crystal: Luminescence dynamics of doped CsMnBr<sub>3</sub>. *J. Chem. Phys.* **1990**, 92, 1768–1774.
- (68) Ferguson, J.; Guggenheim, H. J.; Tanabe, Y. Exchange Effects in the Electronic Absorption Spectrum of Mn(II) in Perovskite Fluorides. *J. Appl. Phys.* **1965**, *36*, 1046–1047.
- (69) Bradshaw, L. R.; May, J. W.; Dempsey, J. L.; Li, X.; Gamelin, D. R. Ferromagnetic excited-state Mn<sup>2+</sup> dimers in Zn<sub>1-x</sub>Mn<sub>x</sub>Se quantum dots observed by time-resolved magnetophotoluminescence. *Phys. Rev. B: Condens. Matter Mater. Phys.* **2014**, 89, 115312.
- (70) De Fontaine, D. The number of independent pair-correlation functions in multicomponent systems. *J. Appl. Crystallogr.* **1971**, *4*, 15–19.
- (71) Yin, W.-J.; Yan, Y.; Wei, S.-H. Anomalous Alloy Properties in Mixed Halide Perovskites. *J. Phys. Chem. Lett.* **2014**, *5*, 3625–3631.
- (72) Tang, W.; Sanville, E.; Henkelman, G. A grid-based Bader analysis algorithm without lattice bias. *J. Phys.: Condens. Matter* **2009**, 21, 084204.
- (73) Beberwyck, B. J.; Surendranath, Y.; Alivisatos, A. P. Cation Exchange: A Versatile Tool for Nanomaterials Synthesis. *J. Phys. Chem. C* **2013**, *117*, 19759–19770.
- (74) De Trizio, L.; Manna, L. Forging Colloidal Nanostructures via Cation Exchange Reactions. *Chem. Rev.* **2016**, *116*, 10852–10887.